Bi-color near infrared thermoreflectometry: A method for true temperature field measurement

Thierry Sentenac, Rémi Gilblas, Daniel Hernandez, Yannick Le Maoult

Bi-color near infrared thermoreflectometry: A method for true temperature field measurement

Thierry Sentenac,[1,2] Rémi Gilblas,[1] Daniel Hernandez,[3] and Yannick Le Maoult[1]
[1]*Université de Toulouse, INSA, UPS, Mines Albi, ISAE, ICA (Institut Clément Ader), Campus Jarlard, F-81013 Albi cedex 09, France*
[2]*Université de Toulouse, CNRS, LAAS, 7 avenue du Colonel Roche, F-31077 Toulouse, France*
[3]*CNRS, PROMES, 7 Rue du Four Solaire, B.P. 5, F-66125 Font Romeu, France*

In a context of radiative temperature field measurement, this paper deals with an innovative method, called bicolor near infrared thermoreflectometry, for the measurement of true temperature fields without prior knowledge of the emissivity field of an opaque material. This method is achieved by a simultaneous measurement, in the near infrared spectral band, of the radiance temperature fields and of the emissivity fields measured indirectly by reflectometry. The theoretical framework of the method is introduced and the principle of the measurements at two wavelengths is detailed. The crucial features of the indirect measurement of emissivity are the measurement of bidirectional reflectivities in a single direction and the introduction of an unknown variable, called the "diffusion factor." Radiance temperature and bidirectional reflectivities are then merged into a bichromatic system based on Kirchhoff's laws. The assumption of the system, based on the invariance of the diffusion factor for two near wavelengths, and the value of the chosen wavelengths, are then discussed in relation to a database of several material properties. A thermoreflectometer prototype was developed, dimensioned, and evaluated. Experiments were carried out to outline its trueness in challenging cases. First, experiments were performed on a metallic sample with a high emissivity value. The bidirectional reflectivity was then measured from low signals. The results on erbium oxide demonstrate the power of the method with materials with high emissivity variations in near infrared spectral band.

I. INTRODUCTION

Infrared thermography is a well established passive noncontact radiometry technique. From the radiance emitted by a material, it only provides a radiance temperature field using Planck's law. The measurement of true temperature fields and its accuracy are completely dependent on the knowledge of the material's emissivity. Unfortunately, the emissivity depends on many parameters including temperature, direction of observation, wavelength, and surface roughness. The challenge becomes serious for the measurement of temperature fields on real two-dimensional objects involved in dynamical processes.[1] The emissivity is unknown for each point on the surface, but, in addition, its value at each point varies during the measurement with the temperature and the material's surface evolution. This paper addresses the problem of the measurement of true temperature field on materials with unknown, selective, and rapidly varying surface emissivity.

For heteropolar dielectric materials (silica, alumina, magnesia, etc.), an elegant method consists in measuring the temperature at Christiansen's point[2] (the wavelength where the material acts as a black body). Christiansen wavelengths are most often located in the mid-infrared (close to 10 μm). Performing thermography at these wavelengths is then possible with a specific filter for each material. Although the Christiansen wavelength depends slightly on temperature and surface, the filter would be effective on a restricted temperature range and a relatively homogeneous surface to minimize the uncertainty in temperature measurement. For gray body and at high temperature, passive methods, bi-color or multi-wavelength real time systems operating in ultraviolet/visible/near infrared (NIR) wavelengths,[3,4] have been developed for temperature field measurements. These methods are based on the gray body assumption which is seldom checked. To overcome the so-called two color assumption, for multi-wavelength systems, an adequate emissivity model can be adapted to various cases under study.[5,6] However, it is impossible to design a universal model that is suitable for surfaces with heterogeneous materials or multi-material surfaces. For all other cases, without making assumptions on the emissivity behavior, the best approach would be to perform an emissivity measurement online and *in situ* simultaneously with the measurement of radiance temperature. Emissivity can be directly measured according to the definition (ratio of material emissivity to black body emissivity).[7] However, for each measurement, the temperature must be specified to calculate emissivity, so the two parameters are dependent. Alternatively, emissivity can be understood by indirect methods through absorptivity or reflectivity measurements. First, photothermal heating methods[8,9] investigate the emissivity measurement through an absorptivity measurement using a powerful light source to heat up the material. But the extrapolation of photothermal methods from a local measurement to a field measurement would require a high power source that it would be very accurately synchronized with the imaging system at a high time resolution. Second, for opaque materials,

directional emissivity and directional-hemispherical reflectivity are linked by Kirchhoff's law. Directional-hemispherical reflectivity requires integrating bidirectional measurements over the entire hemisphere.[10] The complexity of the apparatus and accumulation errors are the major drawbacks of the method for field measurements in working conditions. To avoid the measurement of the directional-hemispherical reflectivity, the introduction of an unknown parameter in Kirchhoff's law, called the "diffusion factor," allows the measurement of reflectivity in a single direction.[11] Some studies[12,13] have implemented this method for point-like measurements through a technique called pyroreflectometry. The advantage is the low power of the laser beam used to generate the reflected flux. This technique seems the most promising way to extrapolate from such point-like measurements to surface measurements.

Based on the same principle of pyroreflectometry, this paper suggests a new technique for measuring true temperature fields, called the bicolor near infrared thermoreflectometry. Indeed, the true temperature field measurement is achieved by measuring simultaneously the radiance temperature field and the bidirectional reflectivity field. These measurements are performed with near infrared imaging detectors associated with low power extended light sources. The name "thermoreflectometry" is related on the one hand to quantitative thermography to describe a technique for mapping spatial temperature (thermograms) and on the other hand to reflectometry to describe the active character of the technique.

The present paper is organized as follows: the first part recalls the theoretical basis and assumptions of thermoreflectometry and highlights the specificities of field measurements. These specificities involve a sensitivity analysis to evaluate the compliance of the assumptions. Given the large number of cases to deal with, this analysis is based on a simulation approach produced from a database of representative materials. The second part reports an extensive statistical analysis of thermoreflectometry. With these results, the third part is devoted to the implementation of the thermorefletometer and the apparatus is described with its calibration procedures. Section V describes the testing and the validation of the method on two representative cases. First, true temperature field measurements are performed on metallic samples which exhibit a high emissivity value. The reflectivity value is then low and its measurement is a challenging case. The other challenging case is to perform measurements on erbium oxide with high emissivity gradients in near infrared spectral band. The measurements are carried out on large area samples at temperatures around 750 °C without knowledge or assumption about the material's emissivity.

II. BACKGROUND OF THEORETICAL BASIS

In the first part, the theoretical basis of the method are recalled and declined for the specifications of a field measurement. Then, as the method must be applicable to any opaque material, a database of thermo-optical properties is built in order to simulate its performances. Its components (emission and reflexion properties), are presented and analyzed in the second part of the section.

A. Problem of radiative temperature measurements

Radiative temperature measurements are based on the analysis of the spectral radiance emitted by the object. For a black body, in the near infrared spectral band, the spectral radiance can be described by Wien's approximation of Planck's law, given by (see the Appendix)

$$L_0(\lambda, T_R) = C_1 \lambda^{-5} \exp\left(\frac{-C_2}{\lambda\, T_R}\right) \quad [\mathrm{W\,sr^{-1}\,m^{-2}\,\mu m^{-1}}]. \quad (1)$$

This approximation is accurate to within 1% if the condition $\lambda\, T_R < 3000\,\mu\mathrm{m\,K}$ is observed. The wavelength should therefore be lower than $2.4\,\mu$m for a temperature range of 300–1000 °C. The black body temperature, called the radiance temperature (T_R), can be directly determined from a radiometer facing the emitting surface.

For a real opaque object at thermal equilibrium, the spectral radiance is equal to the black body radiance calculated at radiance temperature. It is also equal to the product of the spectral emissivity by the black body radiance calculated at the true temperature of the object. The spectral radiance in the $\vec{r}_0$ direction is then written as follows:

$$L^{\vec{r}_0}(\lambda, T) = L_0\left(\lambda, T_R^{\vec{r}_0}\right) = \varepsilon^{\vec{r}_0}(\lambda, T) L_0(\lambda, T). \quad (2)$$

A radiometer, viewing the object under the direction $\vec{r}_0$, always indicates a radiance temperature. The true temperature can only be inferred from the knowledge of the radiance temperature, calculated by a calibration step based on the black body radiance, and from the knowledge of spectral emissivity. Expressing Wien's approximation in Eq. (1), the relation between the true temperature, the radiance temperature, and the spectral emissivity is expressed as follows:

$$\frac{1}{T} = \frac{1}{T_R^{\vec{r}_0}} + \frac{\lambda}{C_2} \ln(\varepsilon^{\vec{r}_0}). \quad (3)$$

The true temperature T is then always higher than the radiance temperature T_R, except for a black body ($\varepsilon^{\vec{r}_0} = 1$) for which both temperatures are equal. From Eq. (3), the relative uncertainty of true temperature with respect to emissivity is given by Eq. (4). Note that the error on radiance temperature is neglected, ($\frac{\Delta T_R^{\vec{r}_0}}{T_R^{\vec{r}_0}} = 0$),

$$\frac{\Delta T}{T} = \frac{\lambda T}{C_2} \frac{\Delta \varepsilon^{\vec{r}_0}}{\varepsilon^{\vec{r}_0}}. \quad (4)$$

In the context of temperature measurements on objects involved in dynamic processes where emissivity is unknown and variable, an active indirect measurement of emissivity is proposed.

B. Background of the physical principle of the thermoreflectometry technique

For an opaque material and following Kirchhoff's laws, the directional spectral emissivity and the directional hemispherical spectral reflectivity obey the following equation:

$$\varepsilon^{\vec{r}_0}(\lambda, T) = 1 - \rho^{\vec{r}_0, \cap}(\lambda, T). \quad (5)$$

The directional hemispherical reflectivity is given by the integration in all directions $\vec{x}$ of the bidirectional reflectivity,

which is carried out over the upward hemisphere, as follows:

$$\rho^{\vec{r}_0,\cap}(\lambda, T) = \int_{\Omega_x=2\pi} \rho^{\vec{r}_0,\vec{x}}(\lambda, T)\cos(\theta_x)d\Omega_x. \quad (6)$$

The physical principle of the thermoreflectometry technique involves the following steps:

- The first step is to perform the measurement of the bidirectional reflectivity in a single direction $\vec{x}_0$, called $\rho^{\vec{r}_0,\vec{x}_0}(\lambda, T)$. The directional hemispherical reflectivity is then expressed with respect to the measured bidirectional reflectivity as follows:

$$\rho^{\vec{r}_0,\cap}(\lambda, T) = \rho^{\vec{r}_0,\vec{x}_0}(\lambda, T) \times \int_{\Omega_x=2\pi} f^{\vec{r}_0,\vec{x},\vec{x}_0}(\lambda, T)\cos(\theta_x)d\Omega_x, \quad (7)$$

  where $f^{\vec{r}_0,\vec{x},\vec{x}_0}$ is the reflection indicator function, which represents normalized values of bidirectional reflectivities.
- The second step is to consider the previous integral as an unknown variable equal to the diffusion factor η as follows:

$$\eta^{\vec{r}_0,\vec{x}_0}(\lambda, T) = \int_{\Omega_r=2\pi} f^{\vec{r}_0,\vec{r},\vec{x}_0}(\lambda, T)\cos(\theta_x)d\Omega_x. \quad (8)$$

  For an opaque material, the diffusion factor is a shape factor, mainly geometrical, and it represents the volume of the bidirectional reflectivities normalized in the reference direction $\vec{x}_0$. It characterizes the proportion of reflected radiation in the direction of measurement with regard to the reflected radiation scattered over the whole hemisphere.

  According to Eqs. (5), (7), and (8) and thanks to Helmholtz's reciprocity theorem applied to bidirectional reflectivity $\rho^{\vec{r}_0,\vec{x}_0}(\lambda, T)$, the emissivity is then expressed as a function of the measured bidirectional reflectivity in a single direction $\vec{x}_0$ and the unknown diffusion factor, as follows:

$$\varepsilon^{\vec{r}_0}(\lambda, T) = 1 - \rho^{\vec{x}_0,\vec{r}_0}(\lambda, T)\eta^{\vec{r}_0,\vec{x}_0}(\lambda, T). \quad (9)$$

  Equation (9) shows that emissivity has a physical sense only if the diffusion factor is positive and less than $1/\rho^{\vec{x}_0,\vec{r}_0}$.
- The third step consists in assuming that the diffusion factor is constant for two wavelengths λ_1 and λ_2

$$\eta^{\vec{r}_0,\vec{x}_0}(\lambda_1, T) = \eta^{\vec{r}_0,\vec{x}_0}(\lambda_2, T). \quad (10)$$

- Finally, the main Eq. (2) is rewritten. The directional emissivity is replaced by Eq. (9) with assumption (10). For two wavelengths, a system of two equations is then introduced as follows:

$$\begin{aligned} L_0\big(\lambda_1, T_R^{\vec{r}_0}(\lambda_1)\big) &= (1 - \rho^{\vec{x}_0,\vec{r}_0}(\lambda_1, T)\eta^{\vec{r}_0,\vec{x}_0}(T))L_0(\lambda_1, T), \\ L_0\big(\lambda_2, T_R^{\vec{r}_0}(\lambda_2)\big) &= (1 - \rho^{\vec{x}_0,\vec{r}_0}(\lambda_2, T)\eta^{\vec{r}_0,\vec{x}_0}(T))L_0(\lambda_2, T). \end{aligned} \quad (11)$$

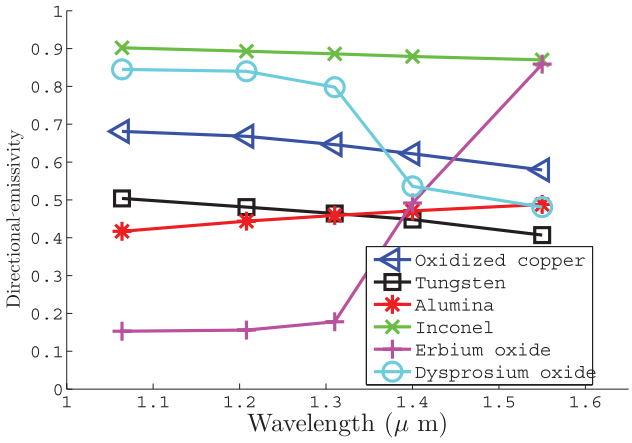

FIG. 1. Directional spectral emissivities of selected samples versus selected wavelengths (1.064, 1.208, 1.310, 1.408, and 1.550 μm) of compatible laser sources.

Measuring radiance temperature and bidirectional reflectivity at two wavelengths, and assuming that shapes of reflectivity distribution are homothetic for both wavelengths, the system of Eq. (11) provides the true temperature and the diffusion factor.

C. Discussion of the method for a database of representative materials

After the presentation of the method and its assumptions, their validity on several representative materials is discussed.

1. Selection of representative samples of materials

A database of representative materials is chosen and composed of thermo-optical properties previously measured in the near infrared spectral band with a Fourier transform spectrometer equipped with an integrating sphere. The directional spectral emissivities of the selected samples, displayed in Figure 1, show that the oxidized copper and tungsten exhibit a metal-like behavior, with a decreasing emissivity with wavelength whereas alumina's emissivity increases. Inconel is a material with very low emissivity decrease which may be assumed to be a gray body. Dysprosium and erbium oxides are spectrally selective materials with high variations of emissivity in both directions.

The database exhibits a wide variety of spectral behaviors and can be considered as a good base for the simulation of the method's behavior.

2. Discussions on bidirectional reflectivities

The database also contains bidirectional reflectivity data. They are measured with a spectrometer equipped with a goniometer enabling the measurement of reflectivity in the incidence plane for a given incident angle and for several reflexion angles. Figure 2 shows that the metal sample of tungsten reflects more for high wavelengths, which is consistent with the decrease in the spectral emissivity. Moreover, this figure shows homothetic reflection lobes for the different

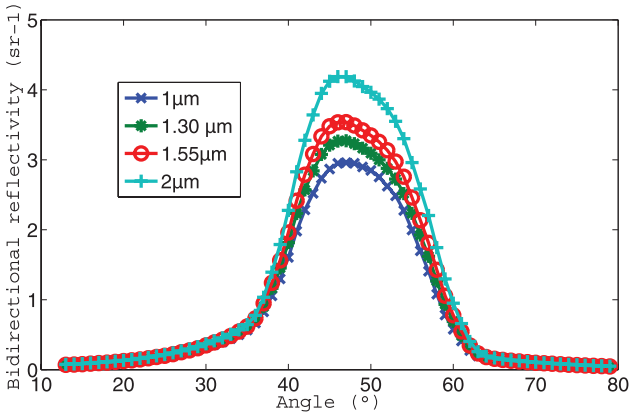

FIG. 2. Bidirectional reflectivities in the incidence plane, with an incident radiation in the direction $\vec{x}_0$ with an angle of 45°, for the sample of tungsten and for four near-infrared wavelengths.

wavelengths. The study of homothety is covered in Sec. II C 3, through the spectral variations in diffusion factor.

Finally, Figure 2 also shows the dependence of the bidirectional reflectivity on the angle of observation: the maximum reflectivity is obtained for an observation angle equal to the incident angle. As shown in Ref. 14, this dependence is particularly marked for specular materials, where light is reflected in a small solid angle. In the case of a field measurement, and for a collimated surface illumination, each pixel has its own direction of observation. As a consequence, the bidirectional reflectivity is different for each pixel and is denoted $\rho^{\vec{x}_0,\vec{r}_0}(\lambda, T, u, v)$. As a conclusion, the bidirectional reflectivity field is predicted as non-uniform, even for homogeneous sample. The more specular the surface is, the more important are in-field variations.

3. Discussions on diffusion factor

For all materials of the database, from Eq. (8) and previous bidirectional reflectivities, the calculated diffusion factor and its relative variation versus the mean value ($\bar{\eta}$), denoted $\eta_r(\lambda) = |\frac{\eta(\lambda)-\bar{\eta}}{\bar{\eta}}|$, are shown in Table I as a function of wavelength.

First of all, the diffusion factor depends on the direction of measurement. If the direction $\vec{x}_0$ is chosen at the maximum of the reflected radiation, the reflection indicator function is in the range [0–1] and the diffusion factor is in the range [0–π]. In the case of a field measurement, the diffusion factor is calculated for each pixel, u, v, of the detector. The normalization direction is then different for each pixel. The value of the diffusion factor depends on each pixel ($\eta^{\vec{r}_0,\vec{x}_0}(T, u, v)$) and it can be greater than π.

Moreover, the diffusion factor depends on surface roughness. For diffuse materials (oxidized copper, Inconel, and alumina), which reflect radiation in many directions, diffusion factors are the highest. On the contrary, for specular materials (tungsten), with a narrow reflection lobe, the diffusion factor is the smallest.

Finally, Table I also shows that for metallic samples (oxidized copper, Inconel, and tungsten) and alumina, the diffusion factor decreases slightly with wavelength (variations do not exceed 5%). It can then be considered as almost constant for all wavelengths. In contrast, for dysprosium and erbium oxides, the diffusion factor variations with wavelength are higher with a maximal variation of 28%.

III. SENSITIVITY OF THERMOREFLECTOMETRY METHOD

This section is devoted to the study of the sensitivity of thermoreflectometry with respect to the behavior of the diffusion factor studied previously, the choice of system parameters (wavelengths values) and the accuracy of system inputs (radiance temperature field and reflectivity field). Experiments are carried out on the previous database and are based on the comparison of the parameters estimated by the method (true temperature fields and diffusion factor fields) and the values used to generate the simulated data. First, the simulation procedure is detailed.

A. Simulation procedure

1. Simulation data

From emissivity and diffusion factor properties and according to Eqs. (3) and (9), the system inputs I (bidirectional reflectivity ($\rho^{\vec{x}_0,\vec{r}_0}$) and radiance temperature (T_R)), tabulated in Table II, are calculated for the maximal temperature of the measuring range (i.e., 1000 °C). According to Eq. (4), this value of true temperature illustrates the worst case for the accuracy of the true temperature.

The variations of bidirectional reflectivities are inverted in relation to emissivity variations. The highest value of reflectivity is recorded for tungsten, due to its specular

TABLE I. Absolute values and relative variations of the diffusion factor versus its mean value $\bar{\eta}$, expressed by $\eta_r(\lambda) = \left|\frac{\eta(\lambda)-\bar{\eta}}{\bar{\eta}}\right|$, for the database materials.

	1.064 μm		1.208 μm		1.310 μm		1.400 μm		1.550 μm	
Materials	$\eta(\lambda)$ (sr)	$\eta_r(\lambda)$ (%)	$\eta(\lambda)$ (sr)	$\eta_r(\lambda)$ (%)	$\eta(\lambda)$ (sr)	$\eta_r(\lambda)$ (%)	$\eta(\lambda)$ (sr)	$\eta_r(\lambda)$ (%)	$\eta(\lambda)$ (sr)	$\eta_r(\lambda)$ (%)
Erbium oxide	1.73	11	1.70	9.07	1.68	7.79	1.55	0.57	1.13	28
Dysprosium oxide	1.81	0.40	1.69	6.10	1.74	3.16	1.88	4.63	1.88	4.24
Alumina	2.16	1.82	2.13	0.22	2.12	0.30	2.11	0.73	2.10	1.01
Inconel	2.04	1.12	2.02	0.08	2.02	0.18	2.00	0.78	2.00	1.53
Oxidized copper	2.04	0.19	2.02	0.92	1.99	0.48	1.98	0.78	1.97	1.53
Tungsten	1.09	4.51	1.05	0.78	1.05	0.08	1.03	1.70	1.01	3.52

TABLE II. Bidirectional reflectivity and radiance temperature for database materials and selected wavelengths.

	1.064 μm		1.208 μm		1.310 μm		1.400 μm		1.550 μm	
Materials	$\rho^{\vec{x}_0,\vec{r}_0}$ (sr^{-1})	T_R (°C)	$\rho^{\vec{x}_0,\vec{r}_0}$ (sr^{-1})	T_R (°C)	$\rho^{\vec{x}_0,\vec{r}_0}$ (sr^{-1})	T_R (°C)	$\rho^{\vec{x}_0,\vec{r}_0}$ (sr^{-1})	T_R (°C)	$\rho^{\vec{x}_0,\vec{r}_0}$ (sr^{-1})	T_R (°C)
Erbium oxide	0.488	809	0.497	789	0.490	788	0.328	897	0.125	974
Dysprosium oxide	0.116	973	0.094	977	0.116	968	0.247	909	0.277	884
Alumina	0.270	903	0.261	898	0.256	895	0.251	892	0.244	886
Inconel	0.048	988	0.053	985	0.056	983	0.061	980	0.065	976
Oxidized copper	0.157	956	0.165	948	0.178	939	0.191	929	0.214	911
Tungsten	0.454	923	0.492	908	0.513	896	0.537	885	0.588	860

behavior. Radiance temperatures are always lower than true temperature. To summarize, for oxidized copper, tungsten, and Inconel: bidirectional reflectivity decreases and radiance temperature increases. The two inputs vary in opposite directions. On the contrary, for alumina, both inputs vary in the same direction, as they both decrease. Considering radiance temperature values, emissivity variations are not strong enough to compensate wavelength variation, which is depicted in Eq. (3). For dysprosium and erbium oxides, the two trends are observed.

Noise is optionally added to each input I by defining $\breve{I}_j = I_j + \nu_j$ where ν is the jth trial value of N trials ($j = 1 \ldots N$) for a random variable following a Gaussian distribution $\mathcal{N}(0, \sigma_x^2)$ of mean zero and standard deviation σ_x.

2. System solution

The solution of system (11) is performed by an optimization algorithm based on the "fsolve" MATLAB function, using the Trust Region Dogleg Algorithm. This algorithm combines a quasi-Newtonian method and a trust region method. The initial values of system parameters are given as follows: (a) according to Eq. (3), true temperature is always higher than radiance temperature. So the initial true temperature T_0 is set to the highest value of radiance temperature $T_0 = max(T_R(\lambda_1), T_R(\lambda_2))$; (b) according to Eq. (9), the diffusion factor must be lower than the inverse of bidirectional reflectivities. So its initial value is $\eta_0 = 1/(max(\rho(\lambda_1), \rho(\lambda_2)))$.

The solution can also be graphically displayed (see Figure 3), considering the diffusion factor as the varying variable. When the curves at two wavelengths cross, estimated true temperatures $\hat{T}$ and diffusion factors $\hat{\eta}$ are retrieved. For two wavelengths λ_1 and λ_2 such as $\lambda_1 < \lambda_2$, if $\rho^{\vec{r}_0,\vec{x}_0}(\lambda_1) < \rho^{\vec{r}_0,\vec{x}_0}(\lambda_2)$ and $T_R(\lambda_1) > T_R(\lambda_2)$ (case of oxidized copper, tungsten, and Inconel), then a single solution exists, as shown in Figure 3.

If $\rho^{\vec{r}_0,\vec{x}_0}(\lambda_1) > \rho^{\vec{r}_0,\vec{x}_0}(\lambda_2)$ and $T_R(\lambda_1) > T_R(\lambda_2)$ (case of alumina), then two solutions are found. A first issue to select the true solution is to consider a third wavelength.[15] A second issue is now being investigated by considering an additional constrained minimization equation and this will be presented in a forthcoming paper.

3. Evaluation criteria

Performances of the resolution method are quantified by computing the usual absolute error of temperature: $E_T = \|T - \hat{T}\|$ where the $\hat{}$ notation represents the estimated value. For errors measured with j noisy data, the mean value

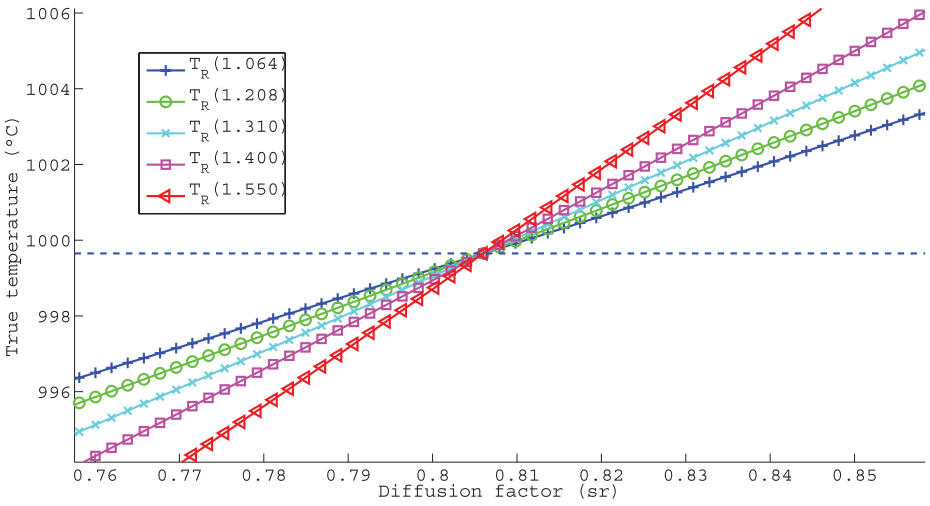

FIG. 3. Graphic resolution of the equation system (11) for oxidized copper with noise-free data.

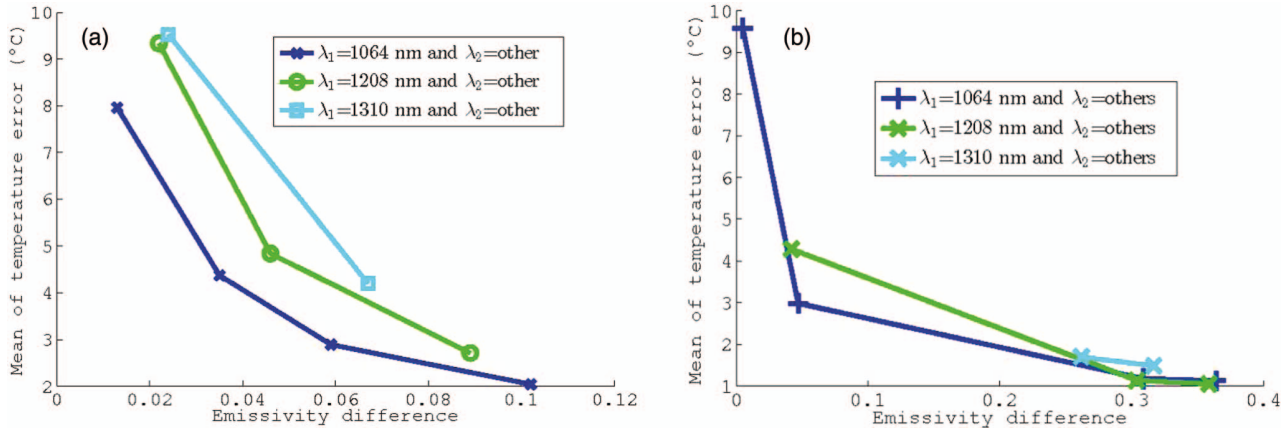

FIG. 4. Mean value of temperature error $\bar{E}_T$ versus emissivity difference for each combination of wavelengths and for oxidized copper (a) and dysprosium oxide materials (b).

$\bar{E}_T$ and the standard deviation σ_{E_T} of the absolute error are calculated on the N trials.

B. Influence of wavelength choice

These first series of simulations are intended to study the influence of the choice of wavelengths λ_1 and λ_2 with the assumption that the diffusion factor is constant between these two wavelengths. The noisy input data, radiance temperature (respectively, bidirectional reflectivity), is generated with a standard deviation of $\sigma_{T_R} = 1\,^\circ$C (respectively, a standard deviation $\sigma_\rho = 0.005\,\mathrm{sr}^{-1}$). The number of trials is set to $N = 100$. Then, for all materials, the system of Eq. (11) is solved for all possible combinations of selected wavelengths. Finally, the mean value of true temperature error $\bar{E}_T$ calculated for oxidized copper (representative case of a metallic material) and dysprosium oxide (representative case of a rare earth) is shown in Figure 4.

The smallest error in temperature is obtained for the highest emissivity difference. It also corresponds to the highest wavelength difference because emissivity variation is monotonous for every material in this database. According to Eqs. (3) and (9), when the values of emissivity are close for the two wavelengths, the values of bidirectional reflectivity and radiance temperature are also close. This suggests that the equations of system (11) cannot be considered as independent for close values of bidirectional reflectivity and radiance temperature. Moreover, for each combination, the highest temperature accuracy is obtained for the smallest value of wavelength ($\lambda_1 = 1.064\,\mu$m) and for a second wavelength, λ_2, which produces the largest difference in emissivity. For all materials, the second wavelength is then equal to $\lambda_2 = 1.550\,\mu$m.

C. Influence of non-compliance of the assumption on the diffusion factor

For wavelengths $\lambda_1 = 1.064$ and $\lambda_2 = 1.550\,\mu$m, the second series of simulations are performed assuming that, on one hand, there are no errors on the inputs of the system but, on the other hand, the diffusion factor varies between the two wavelengths with a maximal relative value of 20%. Under these conditions, Eq. (12) then connects the relative error of temperature and relative error of diffusion factor as follows:

$$\frac{\Delta T}{T} = \frac{\lambda_r \cdot T}{\varepsilon_r \cdot C_2} \frac{\Delta \eta^{\vec{r}_0,\vec{x}_0}}{\eta^{\vec{r}_0,\vec{x}_0}} \tag{12}$$

$$\text{with} \quad \lambda_r = \frac{\lambda_2 \lambda_1}{\lambda_2 - \lambda_1} \quad \text{and} \quad \varepsilon_r = \left| \frac{\varepsilon^{\vec{r}_0}(\lambda_1, T)\varepsilon^{\vec{r}_0}(\lambda_2, T)}{\varepsilon^{\vec{r}_0}(\lambda_1, T) - \varepsilon^{\vec{r}_0}(\lambda_2, T)} \right|.$$

For the two wavelengths ($\lambda_1 = 1.064$ and $\lambda_2 = 1.550\,\mu$m), the critical case is erbium oxide which presents the highest emissivity difference. In contrast, the lowest temperature error is recorded for Inconel sample which exhibits the lowest emissivity variation between the two wavelengths. For erbium oxide sample (respectively, Inconel sample), the relative variation of the diffusion factor $\frac{\Delta \eta^{\vec{r}_0,\vec{x}_0}}{\eta^{\vec{r}_0,\vec{x}_0}}$ has to be less than 8% (respectively, 50%) for a temperature error less than 10 °C. But the variation of the diffusion factor, shown in Table I, is up to 28%. This variation would involve a temperature error of about 30 °C. The assumption on invariance of the diffusion factor has to be especially respected as the emissivity variation between the two wavelengths is large.

D. Robustness to radiance temperature and bidirectional reflectivity noise

The two previous conclusions are opposed to each other. The chosen wavelengths have to be as far as possible to comply with the system's conditioning. In contrast, they have to be as close as possible to avoid diffusion factor variations, which can involve significant errors in temperature measurement.

This trade-off is solved by the choice of wavelengths $[1.310-1.550]\,\mu$m. The small difference between the two wavelengths fosters compliance of the invariance of the diffusion factor. Moreover, relatively high near-infrared wavelengths enable low temperatures to be measured (up to 500 °C).

For the wavelengths combination ($\lambda_1 = 1.310$ and $\lambda_2 = 1.550\,\mu$m), the third simulation series aims to test the

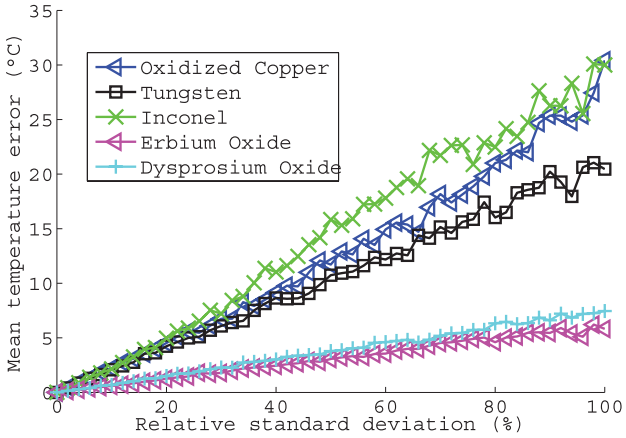

FIG. 5. Mean value of temperature error $\bar{E}_T$ versus the normalized standard deviation (i.e., 100% represents 5 °C (respectively, 0.01 sr^{-1})) for the standard deviation of radiance temperature (respectively, bidirectional reflectivity).

robustness of the method to noisy inputs. A number N of 500 trials of inputs were processed with a noise standard deviation of radiance temperature σ_{T_R} (respectively, bidirectional reflectivity σ_ρ) from 0 to 5 °C (respectively, from 0 to 0.01 sr^{-1}). The mean value of temperature error $\bar{E}_T$ is plotted in Figure 5 versus the normalized standard deviation.

In accordance with previous results, mean value of temperature error increases twice as fast for metallic materials as it does for erbium and dysprosium oxides. The measurement of true temperature with 10 °C accuracy at 1000 °C can only be achieved, in the worst case (on metallic samples), if the measurement of radiance temperature (respectively, bidirectional reflectivity) is done with a standard deviation of noise around 1.8 °C (respectively, around 0.0038 sr^{-1}). In contrast, for erbium and dysprosium oxides, the same requirement is reached only for a noise standard deviation on temperature of 8 °C and on bidirectional reflectivity of 0.015 sr^{-1}. These results illustrate the extended requirements of the method, and the prototype described in Sec. IV will have to satisfy this requirement for accuracy.

IV. BICOLOR NEAR INFRARED THERMOREFLECTOMETER

The stages of the experimental thermoreflectometer's development are declined in this section. Its associated radiometric and reflectometric calibrations are also detailed.

A. Experimental thermoreflectometer

The experimental thermoreflectometer involves laser sources, a filter wheel, a near infrared camera, and a data acquisition and control system. The laser sources, required for bidirectional reflectivity measurements, are continuous with an adjustable power between 0 and 20 mW and centered on 1.310 and 1.550 μm. The two monochromatic rays are optically coupled, and emerge from the same beam expander. Thanks to this enlargement, a 5 cm diameter, bicolor, and collimated beam is provided at a distance of 1 m. The filter wheel is motorized and selects the working spectral band of the camera. The filters mounted on the wheel are centered at a wavelength of 1.310 or 1.550 μm with a bandwidth of 50 nm. The camera is a near infrared camera equipped with a InGaAs detector with a pixel resolution of 320 × 256 pixels. The digital levels (DL) of the camera signal are expressed over 12 bits. Its spectral response ranges from 0.9 to 1.7 μm. The control of integration time (ti), between 1 μs and 1 s, enables the acquisition of a high dynamic range of measurement. The camera is then configured in such a way as to avoid a signal level lower than the noise level and the overexposure of the detector. The camera is equipped with a 50 mm focal length lens. The field of view of the camera is 20 × 20 cm and the spatial resolution, an area of the sample corresponding to a pixel, is about 0.4 mm. The data acquisition system controls the position of the filter wheel and supplies voltage to the laser sources. It also acquires camera signals for radiance temperature and bidirectional reflectivity measurements.

B. Thermoreflectometer signals

Each pixel of the camera of coordinates u and v converts the incident flux as a signal expressed in DL. The signal of each pixel is assumed to be independent from its neighborhood.

During the passive phase of the measurement (laser source off), each pixel supplies a thermal signal in the $\vec{r}_0$ direction, denoted $I_E^{\vec{r}_0}(u,v)$, which is proportional to the heat flux emitted by the object. However, this signal also suffers from the dark current signal, denoted $\bar{I}_{dark}(u,v)$, and from temporal noise sources. The effects of temporal noise are minimized by averaging the signal on several frames (in practice 50 frames), denoted $\bar{I}_E$. The dark signal is measured with a shutter placed in front of the camera and is then subtracted. Finally, the thermal signal of interest, denoted $\bar{Ic}_E^{\vec{r}_0}$, used to measure the radiance temperature, is normalized by the integration time and it is expressed by Eq. (13) as follows:

$$\bar{Ic}_E^{\vec{r}_0}(u,v) = \frac{\bar{I}_E^{\vec{r}_0}(u,v) - \bar{I}_{dark}^{\vec{r}_0}(u,v)}{ti}. \tag{13}$$

During the active phase of the measurement (laser source on), each pixel provides a signal denoted $I_{E+R}^{\vec{x}_0,\vec{r}_0}$. This signal is the sum of the signal proportional to the heat flux emitted ($\bar{I}_E^{\vec{r}_0}$) and the signal from the flux reflected by the object. The mean reflected signal of interest, $\bar{Ic}_R$, used to measure the bidirectional reflectivity, is then given by Eq. (14)

$$\bar{Ic}_R^{\vec{x}_0,\vec{r}_0}(u,v) = \frac{\bar{I}_{E+R}^{\vec{x}_0,\vec{r}_0}(u,v) - \bar{I}_E^{\vec{r}_0}(u,v)}{ti}. \tag{14}$$

From these signals of interest, each pixel of the thermoreflectometer must be calibrated as a radiometer and a reflectometer.

C. Radiometric calibration

From a radiometric point of view, the thermal signal of interest $\bar{Ic}_E^{\vec{r}_0}$ is related to the radiance temperature $T_R^{\vec{r}_0}$ using Wien's law (see Eq. (1)). The radiometric model then

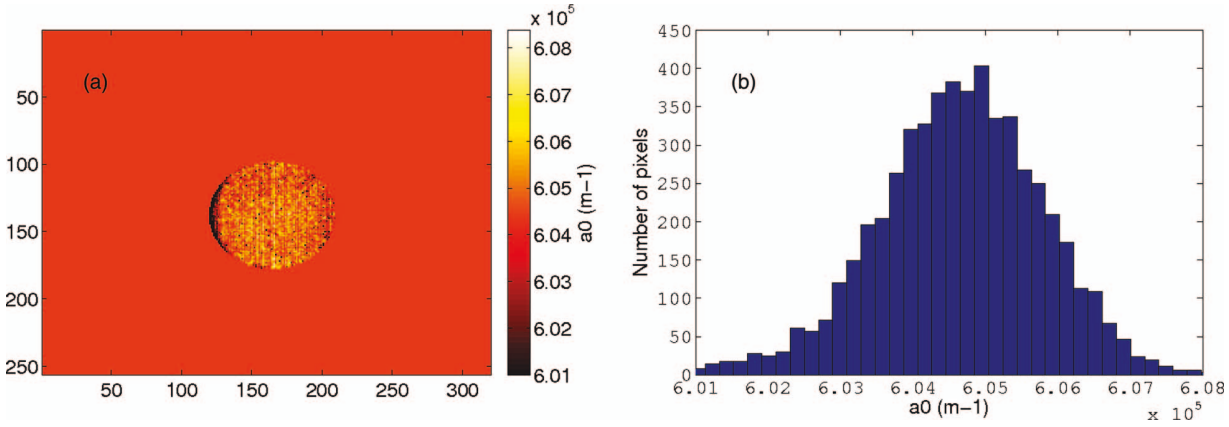

FIG. 6. Images (a) and associated histogram (b) of parameter a_0 of Eq. (15) for a filter centered at a wavelength of 1.550 μm and with a bandwidth of 50 nm.

describes the relation between the radiance temperature and the signal. It allows a radiance thermal map ($T_R^{\vec{r}_0}(u, v)$) to be computed from an image acquired by the camera. Finally, the radiometric model parameters are computed using a radiometric calibration procedure.

1. Radiometric model

In the NIR spectral band, a specific radiometric model is required[16,17] and is given by Eqs. (15) and (16)

$$\bar{Ic}_E^{\vec{r}_0}(u, v) = A_2(u, v) \exp\left(\frac{-C_2}{\lambda_x(u, v) \times T_R^{\vec{r}_0}(u, v)}\right) \quad (15)$$

with:

$$\frac{1}{\lambda_x(u, v)} = \left(a_0(u, v) + \frac{a_1(u, v)}{T_R^{\vec{r}_0}(u, v)}\left(+ \frac{a_2(u, v)}{T_R^{\vec{r}_0 2}(u, v)}\right)\right). \quad (16)$$

The parameter A_2 is assumed to be a property of the camera that only depends on its spectral characteristics and its spectral responsivity. The extended effective wavelength λ_x is a polynomial function of the inverse of the temperature.[18] The parameter definitions of this function, provided in the paper,[19] show that a_0 and a_1 explicitly depend on the spectral response and the shape of the filter, and that the parameter a_2 is theoretically zero for narrow bandwidth filter. The order of the polynomial function then depends on the bandwidth of the filter: the wider the spectral band of the filter is, the higher the function's order of the extended effective wavelength has to be.

Finally, all radiometric model parameters are intrinsic to each pixel of coordinates u and v and consist therefore in four images ($A_2(u, v)$, $a_0(u, v)$, $a_1(u, v)$, ($a_2(u, v)$)). Each pixel is then calibrated during the radiometric calibration process.

2. Radiometric calibration process

First, the fitting of parameters of Eq. (15) requires some known reference radiance temperatures. They are provided by a black body cavity in the range [500–900] °C, with a diameter of 50 mm and an emissivity of 0.995. The calibration process is carried out for a camera equipped with filters centered at wavelengths 1.310 and 1.550 μm and with a bandwidth of 50 nm.

The parameter image $a_0(u, v)$ and its associated histograms are shown in Figure 6. The parameter value is computed for each pixel of the area illuminated by the black body. Otherwise, the parameters are equal to the mean spatial value of parameters calculated on the pixels in the area of the black body, denoted $\tilde{a_0}$. It should be noted that the pixels outside of the area of the black body are not strictly calibrated. As they behave like the mean of the central pixels, their measurements will not be corrected from the differences in photoresponses of each pixel. The mean values of the calibration parameters $\tilde{A_2}$, $\tilde{a_0}$, and $\tilde{a_1}$ and for both filters are gathered in Table III. These values highlight the low spatial dispersion of pixel responsivities. The lowest variation is observed on the parameter a_0 which sets the value of the extended effective wavelength. The inverse of the mean value of the parameter $\tilde{a_0}$ is homogeneous to a wavelength that is equal to the mean wavelength of filters (1.310 and 1.550 μm).

Finally, the temperature uncertainty of the radiometric calibration procedure was characterized by placing the black body in front of the thermoreflectometer a second time. For the highest calibration temperature of 900 °C, the thermal signal of interest was recorded. From its signal, the true temperature $\hat{T}(u, v)$ is estimated by solving polynomial relation (15) using previous parameters of the radiometric calibration. This procedure was performed on a series of measurement to consider the possible slight temporal variation of the black body. The histogram of the temperature difference between the estimated and the black body temperature ($E_T = |T - \hat{T}(u, v)|$),

TABLE III. Spatial mean and standard deviation of radiometric calibration parameters for wavelengths $\lambda_1 = 1.310$ and $\lambda_2 = 1.550$ μm and with a spectral bandwidth of $\Delta\lambda = 50$ nm.

Wavelength [nm]	x	A_2 [DL m^4 s^{-1}]	a_0 [m^{-1}]	a_1 [K m^{-1}]
$\lambda_1 = 1310$	$\tilde{x}$	1.89×10^9	6.97×10^5	3.23×10^7
	σ_x	1.20%	0.24%	2.97%
$\lambda_2 = 1550$	$\tilde{x}$	9.68×10^9	6.05×10^5	1.79×10^7
	σ_x	1.06%	0.20%	3.68%

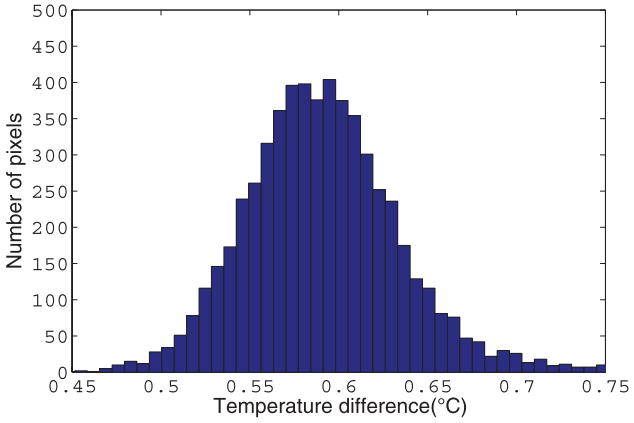

FIG. 7. Histogram of difference between the estimated temperature and the black body temperature ($E_T = |T - \hat{T}(u,v)|$) at 900 °C for the filter centered at wavelength 1.550 μm.

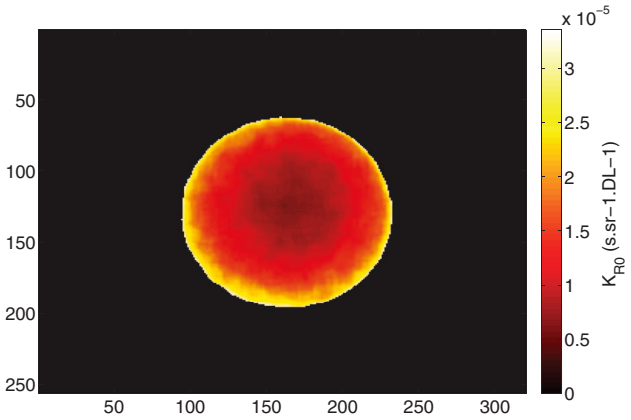

FIG. 8. Calibration parameter $K_{R0}^{\vec{x}_0,\vec{r}_0}$ for wavelength $\lambda = 1.550\,\mu$m.

is plotted as a function of the black body temperature in Figure 7.

The mean temperature difference is equal to $\tilde{E}_T = 0.99\,^\circ$C with a standard deviation of 5% at wavelength 1.310 μm (and, respectively, $\tilde{E}_T = 0.59\,^\circ$C with a standard deviation of 8% at wavelength 1.550 μm). The temperature difference with the suggested radiometric model at first order is low for both wavelengths (inferior or equal to 1 °C). It is lower than that recommended in Sec. III D and it would achieve an uncertainty on true temperature of 4 °C at 1000 °C.

D. Reflectometric calibration

The reflectometric model relating the reflected signal and the bidirectional reflectivity is detailed below and its calibration process and accuracy are also discussed.

1. Reflectometric model

The extended monochromatic optical source emits from a surface S_a a collimated beam in direction $\vec{x}_0$. This beam intercepts the object under study with an apparent surface $dS_a \cos\theta_{x_0}$, and rays are reflected in all directions. The radiance detected by a pixel is relative to the illumination of a surface element corresponding to each projection of the pixels in the object's plane, written $E^{\vec{x}_0}$. Finally, Eq. (17) relates the pixel's signal $\bar{I}c_R^{\vec{x}_0,\vec{r}_0}$, a strictly monochromatic coefficient A_3 relative to each pixel of the camera, and the bidirectional reflectivity $\rho^{\vec{x}_0,\vec{r}_0}$

$$\bar{I}c_R^{\vec{x}_0,\vec{r}_0}(u,v) = A_3(u,v)\,\rho^{\vec{x}_0,\vec{r}_0}(u,v)\,E^{\vec{x}_0}(u,v). \qquad (17)$$

The reflectometric model is linear with incident illumination and therefore depends on the intensity of the source and the angle between the source and the surface normal.

2. Reflectometric calibration process

The thermoreflectometer is then set in front of a diffuse calibrated standard reflector (Spectralon) with known bidirectional reflectivity, $\rho_0^{\vec{x}_0,\vec{r}_0}$. For wavelengths from 0.9 to 1.7 μm, $\rho_0^{\vec{x}_0,\vec{r}_0}$ is constant for Spectralon and equal to 0.392 sr^{-1} (see Ref. 20). The reference reflected signal, $\bar{I}c_{R0}^{\vec{x}_0,\vec{r}_0}$, is recorded for wavelengths 1.310 and 1.550 μm and the single calibration parameter $K_{R0}^{\vec{x}_0,\vec{r}_0}$ is then deducted by the following ratio:

$$K_{R0}^{\vec{x}_0,\vec{r}_0}(u,v) = A_3(u,v)\,E^{\vec{x}_0}(u,v) = \frac{\rho_0^{\vec{x}_0,\vec{r}_0}}{\bar{I}c_{R0}^{\vec{x}_0,\vec{r}_0}(u,v)}. \qquad (18)$$

Figure 8 shows the coefficient $K_{R0}^{\vec{x}_0,\vec{r}_0}$ for a laser source emitting at 1.550 μm with a continuous optical power of 20 mW, and with an angle from the surface of about 13°. First of all, only a part of the matrix is illuminated, so only the pixels corresponding to the laser spot are calibrated. The laser provides a Gaussian power distribution along the direction perpendicular to the propagation one. The surface is not illuminated uniformly and the values of $K_{R0}^{\vec{x}_0,\vec{r}_0}$ are thus not uniform along the spot. As $K_{R0}^{\vec{x}_0,\vec{r}_0}$ is inversely proportional to the camera signal, it exhibits an inverse Gaussian shape. This characteristic is not problematic as long as this trend stays the same between the calibration step and the measurement step.

Finally, to analyze the calibration accuracy, the Spectralon plate is again placed in front of the thermoreflectometer. The voltage supplied to the lasers remains the same. From the field measurement of signals reflected from it, the estimated bidirectional reflectivity $\hat{\rho}^{\vec{x}_0,\vec{r}_0}$ is inferred by inverting Eq. (18). Figure 9 displays, on the left, the image of the estimated bidirectional reflectivities, and on the right, a histogram of the difference between estimated and Spectralon values ($E_\rho = (\rho_0^{\vec{x}_0,\vec{r}_0} - \hat{\rho}^{\vec{x}_0,\vec{r}_0}(u,v))$), at a wavelength of 1.550 μm.

The images of bidirectional reflectivities show a good uniformity and the mean value corresponds to the Spectralon's bidirectional reflectivity. The histogram demonstrates a spatial mean reflectivity difference of $\tilde{E}_\rho$ around 0 with a standard deviation of 2.4×10^{-3} sr^{-1} for wavelength 1310 μm (and, respectively, 3.11×10^{-3} sr^{-1} for wavelength 1550 μm). These results comply with Sec. III requirements.

In the next part, the fully calibrated system will be tested and evaluated on real measurements.

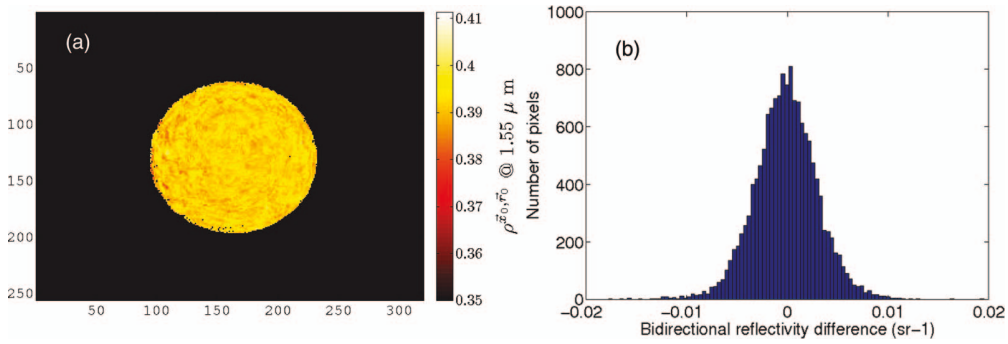

FIG. 9. Image of bidirectional reflectivities (a) and histogram of differences between estimated and real bidirectional reflectivities (b) for $\lambda = 1.550\,\mu$m.

V. EXPERIMENTS

As shown in Figure 5, two behaviors were highlighted for the measurement error of true temperature for the materials studied. First, metallic materials exhibit a low emissivity gradient with the highest expected measurement error. The sample of Inconel represents the worst case of measurement because its emissivity decreases slowly with wavelength and its value is very high. Consequently, its bidirectional reflectivities are the lowest of all metallic samples. Second, rare earth oxides show a high spectral emissivity variation with a low measurement error. The sample selected is erbium oxide because its emissivity increases with wavelength. This section is then devoted to the measurement of true temperature fields for these two representative samples.

A. Experimental setup

As shown in Figure 10, the sample (item 1) is heated on its rear face by a plate (item 3) and is leaned against it thanks to two beveled edges (item 2). The plate can reach temperatures up to 850 °C. The surface reference temperature is given by thermocouples welded on the front face or bonded inside the sample. The thermoreflectometer is located approximately at a distance of 1 m. The lasers emit with an incident angle of 13° with respect to the normal of the sample. Measurements of radiance temperature and bidirectional reflectivity are carried out at two wavelengths $\lambda_1 = 1.31$ and $\lambda_2 = 1.550\,\mu$m. Acquisitions, commands, and processing are performed by a computer.

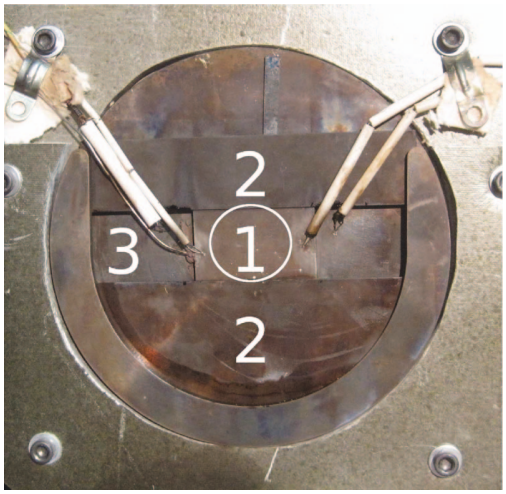

FIG. 10. Inconel sample instrumentation (item 1 is the measured sample, item 2 is the two beveled edges, item 3 is the plate used to heat the rear face of the sample, and the white circle is the ROI).

B. Results on Inconel sample with low emissivity gradient

True temperature measurements were carried out on Inconel sample under air. The oxide layer formed during heating is assumed to be constant over the time of the measurement. The sample thickness is 6 mm and its surface is 15 cm^2 (see Figure 10). The sample is heated to a reference temperature of $T_{ref} = 732\,^\circ$C given by the thermocouple inside the sample. For this experiment, measurement will be carried out on the area materialized by a white circle on Figure 10, denoted region of interest (ROI). The images presented are then a zoom in this ROI.

1. Field measurement of radiance temperature

The first step of the method is the measurement of the radiance temperature field at two wavelengths in the ROI. The radiance temperature field at λ_2 is shown in Figure 11, on the left, with a mean spatial value of $\tilde{T}_R(\lambda_2) = 723\,^\circ$C and a standard deviation $\sigma_{T_R}(\lambda_2) = 3\,^\circ$C. As emissivity is uniform along the sample, these spatial variations are attributed to the heating non-uniformity.

According to Eq. (3) and the results of Table IV, the values of radiance temperatures are lower than the reference temperature. Moreover, as shown in Figure 1, Inconel emissivity decreases with wavelength, so the mean spatial value of radiance temperature $\tilde{T}_R$ is lower at λ_1 than at λ_2 ($\tilde{T}_R(\lambda_1) > \tilde{T}_R(\lambda_2)$). This result is highlighted by Figure 11, on the

TABLE IV. Results on Inconel sample heated at 732 °C.

	$\tilde{x}(\lambda_1)$	$\sigma_x(\lambda_1)$	$\tilde{x}(\lambda_2)$	$\sigma_x(\lambda_2)$
$x = \rho^{\vec{x}_0,\vec{r}_0}(\mathrm{sr}^{-1})$	0.029	0.006	0.035	0.008
$x = T_R(^\circ\mathrm{C})$	726	3	723	3
$x = \varepsilon^{\vec{r}_0}$	0.921	0.029	0.910	0.025

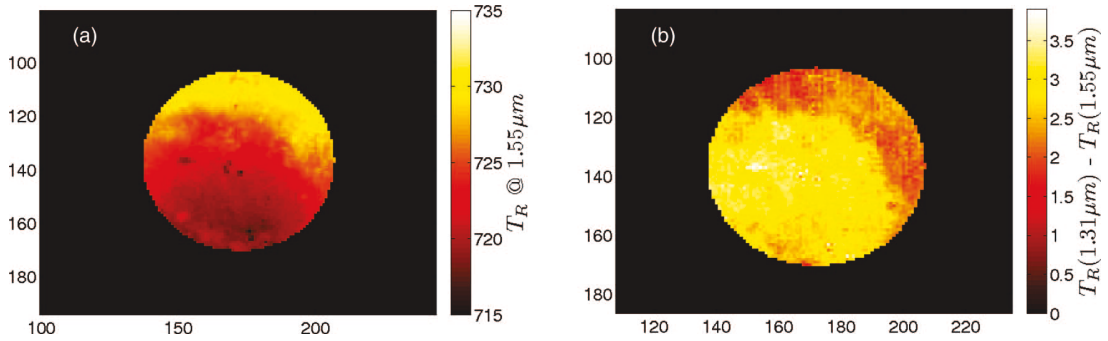

FIG. 11. Field measurement of radiance temperatures (a) at λ_2 and image of the difference of radiance temperature fields for both wavelengths (b).

right, which shows the image of the differences between the radiance temperature measured at λ_1 and the one measured at λ_2. Its values are positive for each pixel of the ROI, thus proving that emissivity decreases with wavelength all along the surface.

2. Field measurement of bidirectional reflectivity

The second step of the thermoreflectometry method is to measure the bidirectional reflectivity field at two wavelengths. In agreement with the emissivity values of Inconel (see Figure 1), Figure 12 demonstrates the low values of bidirectional reflectivities which are consistent with the values of Sec. III (see Table II). Mean spatial values of bidirectional reflectivity recorded on the spot laser area are: $\tilde{\rho}^{\vec{x}_0,\vec{r}_0}(\lambda_1) = 2.9 \times 10^{-2}\,\mathrm{sr}^{-1}$ and $\tilde{\rho}^{\vec{x}_0,\vec{r}_0}(\lambda_2) = 3.5 \times 10^{-2}\,\mathrm{sr}^{-1}$ (see Table IV). The standard deviation around these mean reflectivity values at both wavelengths is equal to $\sigma_\rho(\lambda_1) = 6.3 \times 10^{-3}\,\mathrm{sr}^{-1}$ (resp. $\sigma_\rho(\lambda_2) = 8.2 \times 10^{-3}\,\mathrm{sr}^{-1}$). This variation of about 25% is mainly due to the different observation angles for each pixels. As shown in Figure 2, bidirectional reflectivity depends on directions (of incidence and observation) of the experimental configuration. As a consequence, for each pixel's coordinates, the bidirectional reflectivity detected is specific.

Moreover, the value of reflectivity is higher at λ_2 than at λ_1 ($\tilde{\rho}^{\vec{x}_0,\vec{r}_0}(\lambda_1) < \tilde{\rho}^{\vec{x}_0,\vec{r}_0}(\lambda_2)$). This behavior is consistent with the decrease in emissivity with wavelength and it is the same for all metallic materials.

3. Computation of true temperature fields

Once bidirectional reflectivity and radiance temperature fields are measured, the third step is to calculate the true temperature and the diffusion factor fields by solving the system introduced in Eq. (11). As shown by Figure 13, the true temperature field, an image of 3277 pixels of the laser spot, follows the non-uniformity of the sample's heating, which is warmer at the top of the sample. The spatial mean value is centered on $\tilde{T} = 734\,^\circ\mathrm{C}$ and the spatial standard deviation around this mean value is $\sigma_T = 4\,^\circ\mathrm{C}$. This spatial dispersion is close to that measured on radiance temperature $\sigma_{T_R}(\lambda_2) = 3\,^\circ\mathrm{C}$. The spatial mean value is also very close to the reference temperature ($T_{ref} = 732\,^\circ\mathrm{C}$).

4. Computation of emissivity fields

The last step is the computation of the emissivity field, which enables the validation of the method. Indeed, the method provides the diffusion factor fields with a spatial mean values on the spot area of $\tilde{\eta} = 2.76$ sr and its associated spatial standard deviation of $\sigma_\eta = 1.0$ sr. According to Eq. (9), the spatial variations of the diffusion factor are identical to that of bidirectional reflectivity, so they can reach 25% of the mean value. Moreover, according to this equation, the value of the emissivity field can be inferred. Their spatial mean values calculated on the spot area and their spatial standard deviation around these values are tabulated in Table IV.

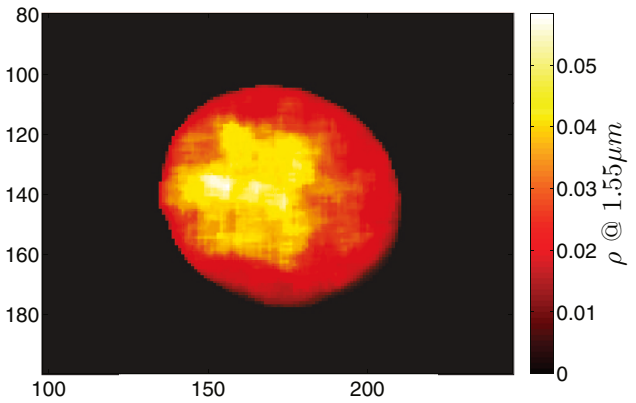

FIG. 12. Field measurement of bidirectional reflectivities at λ_2.

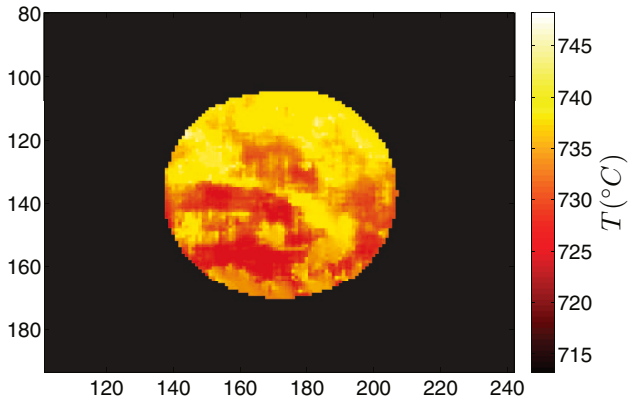

FIG. 13. True temperature field of Inconel sample.

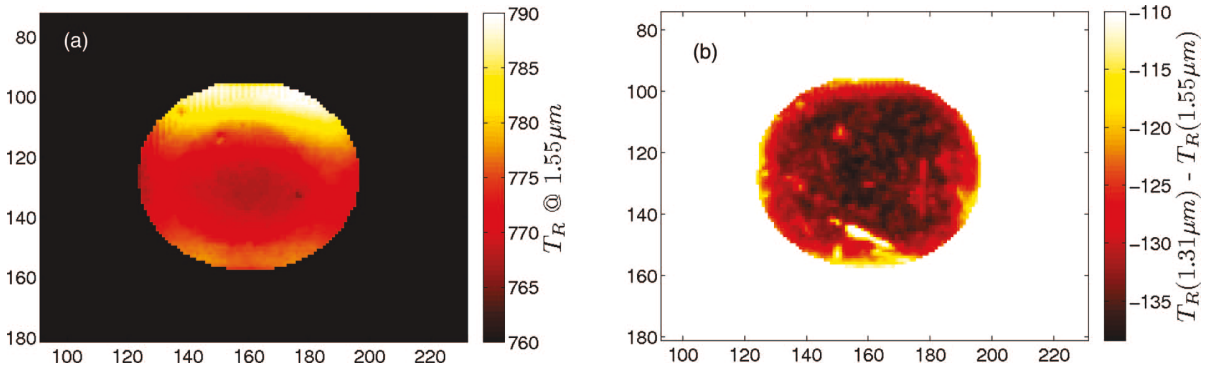

FIG. 14. Field measurement of radiance temperatures at λ_2 (a) and image of the difference of radiance temperature fields for both wavelengths (b).

The values calculated are consistent with the values measured by the spectrometer (see Figure 1). Nevertheless, emissivities calculated by thermoreflectometry at 732 °C are higher than the values measured by the spectrometer at room temperature of about 0.04. This behavior is consistent with the typical increase of emissivity with temperature for metals. Consequently, this last calculation fully validates every step of the method.

Finally, for materials with a low emissivity gradient such as Inconel, despite the difficult conditions of reflectivity measurement, the thermoreflectometry provides an accurate true temperature field with an accuracy on the spatial mean value of around 2 °C.

C. Results on erbium oxide sample with a high emissivity variation

The performances of thermoreflectometry are now analyzed on a very spectrally selective material: erbium oxide. The sample is a 3 cm diameter disc with 4 mm thickness. It is heated to a reference temperature of 795 °C.

The image of radiance temperature at λ_2 is presented in Figure 14, on the left. Its mean spatial value is $\tilde{T}_R(\lambda_2)$ = 775 °C and its associated standard deviation is $\sigma_{T_R}(\lambda_2)$ = 6 °C. Like for the Inconel sample, these values testify once again the non-uniformity of surface temperature, which constitutes the minimum non-uniformity of the final true temperature field. The mean values of radiance temperatures are $\tilde{T}_R(\lambda_1) = 644\,^{\circ}\mathrm{C}$ for λ_1 (respectively, $\tilde{T}_R(\lambda_2) = 775\,^{\circ}\mathrm{C}$ for λ_2). These variations are due to the strong variations in emissivity for erbium oxide at the wavelengths chosen. This phenomenon is emphasized by Figure 14, on the right, which represents the image of radiance temperature difference between wavelength λ_1 and λ_2. Unlike Figure 11, Figure 14 exhibits a negative and high value of the difference. This means that the radiance temperature at λ_1 is lower than that at λ_2 for each pixel, which is very consistent with the emissivity spectral variation.

Figure 15 shows the image of bidirectional reflectivity at λ_1. The means values are: $\tilde{\rho}^{\vec{x}_0,\vec{r}_0}(\lambda_1) = 2.9 \times 10^{-1}\ \mathrm{sr}^{-1}$ and $\tilde{\rho}^{\vec{x}_0,\vec{r}_0}(\lambda_2) = 4.8 \times 10^{-2}\ \mathrm{sr}^{-1}$. In this case, in agreement with emissivity behavior, spatial mean reflectivity at λ_2 is lower than at λ_1.

Figure 16 shows the true temperature of each pixel. The mean value of true temperature is equal to 793 °C, which is very consistent with the reference temperature (T_{ref} = 795 °C). The spatial standard deviation around this mean value is σ_T = 9 °C. This variation corresponds to the non-uniform heating, which is depicted by a pattern with maximum values on the upper part of the sample.

Finally, despite the large variation in emissivity, the method provides an accurate estimation of true temperature as shown in Sec. III. The results of the estimated emissivity values, tabulated in Table V, are also consistent with those obtained by spectroscopy (see Figure 1). Finally, for materials

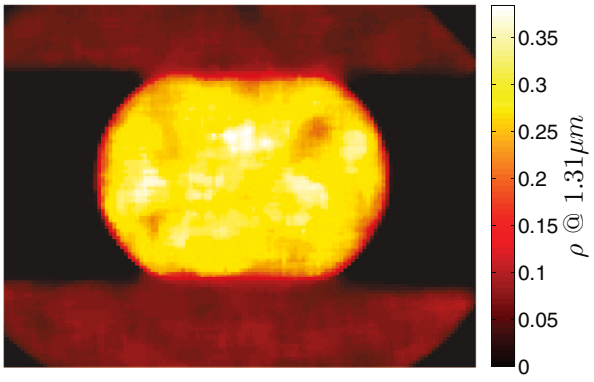

FIG. 15. Image of bidirectional reflectivity field for erbium oxide sample at λ_1.

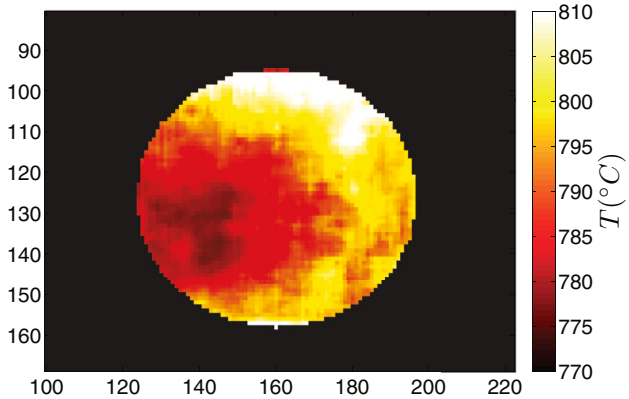

FIG. 16. True temperature field of erbium oxide sample.

TABLE V. Results on erbium oxide sample heated at 795 °C.

	$\tilde{x}(\lambda_1)$	$\sigma_x(\lambda_1)$	$\tilde{x}(\lambda_2)$	$\sigma_x(\lambda_2)$
$x = \rho^{\vec{x}_0,\vec{r}_0}(\mathrm{sr}^{-1})$	0.288	0.036	0.048	0.013
$x = T_R(^\circ\mathrm{C})$	644	9	775	6
$x = \varepsilon^{\vec{r}_0}$	0.185	0.018	0.861	0.043

with a high emissivity gradient, known as a difficult case of non-contact temperature measurement, the thermoreflectometry method demonstrates its good performances experimentally.

VI. CONCLUSION

In this paper, the method of thermoreflectometry has been described for non-contact true temperature field measurements on any kind of opaque plane sample and without prior knowledge of surface emissivity. This capability is achieved thanks to simultaneous measurements of the sample thermal signal through the radiance temperature (thermography) and of its emissivity with an indirect method (reflectometry). The main interest of the method is to obtain the ratio of emissivities for two wavelengths by measuring bidirectional reflectivities in only one direction. This approximation is compensated by the introduction of an unknown variable called the diffusion factor. The fields of true temperature and diffusion factor are then computed thanks to the resolution of a bichromatic system based on the assumption of invariance of the diffusion factor for these two wavelengths.

Section III demonstrated that, on the one hand, the two wavelengths have to be as far as possible in the near infrared spectral band in order to favor the conditioning of the system. On the other hand, wavelengths have to be as close as possible so that the diffusion factor is kept constant. This compromise is solved by choosing wavelengths $\lambda_1 = 1.310$ and $\lambda_2 = 1.550\,\mu$m. In this configuration, the accuracy on true temperature reaches 10 °C at 1000 °C if the accuracy on radiance temperature is less than 1.8 °C and on bidirectional reflectivity less than 0.0038 sr^{-1}.

The experimental device, presented in Sec. IV, consists of a NIR camera, laser sources, and a spectral selection enabled by a motorized filter wheel. After a calibration step, the radiance temperature measurement is performed with a specific NIR model which leads to an uncertainty of less than 1 °C. The bidirectional reflectivity measurement includes a linear model involving a mean uncertainty of 3.1 $\times\ 10^{-3}\ \mathrm{sr}^{-1}$. Uncertainty on the true temperature will then be less than 8 °C, which is compatible with the requirements expressed.

The results obtained in Sec. V on an Inconel sample, which represents a case with a very high emissivity, demonstrated that thermoreflectometry is relevant in determining the true temperature field with a spatial mean value very close to the reference temperature (a difference of around 2 °C). The thermoreflectometry was also tested on an erbium oxide sample, which represents a rare earth behavior with very strong emissivity variations in the near infrared. This material is considered as a critical case for any classic quantitative thermography instrument. However, thermoreflectometry behaved correctly and the accuracy was once again very good with a temperature difference between the surface temperature provided and the reference temperature of around 2 °C with a time resolution of 200 ms.

ACKNOWLEDGMENTS

This work was carried out in R3T (Real Time True Temperature) project, supported by the French National Research Agency.

APPENDIX: GLOSSARY

Symbol	Name	Unit	Symbol	Name	Unit
$\cap$	Solid angle of the hemisphere	2π sr	$f^{\vec{i}_0,\vec{r},\vec{r}_0}$	Reflexion indicator	
$\varepsilon^{\vec{i}_0}$	Directional emissivity		$I^{\vec{i}_0,\vec{r}_0}$	Digital camera signal	DL
$\eta^{\vec{i}_0,\vec{r}_0}$	Diffusion factor	sr	$\vec{i}_0, \vec{r}_0$	First, second reference direction	
λ	Wavelength	μm	$K_{ref}^{\vec{i}_0,\vec{r}_0}$	Reflectometric calibration coefficient	$\mathrm{sr}^{-1}\,\mathrm{DL}^{-1}$
$\rho^{\vec{i}_0,\cap}$	Directional hemispheric Reflectivity		L_0	Black body radiance	$\mathrm{W\,sr^{-1}m^{-2}}\,\mu\mathrm{m}^{-1}$
$\rho^{\vec{i}_0,\vec{r}_0}$	Bidirectional reflectivity	sr^{-1}	$L^{\vec{i}_0}$	Directional radiance	$\mathrm{W\,sr^{-1}\,m^{-2}}\,\mu\mathrm{m}^{-1}$
$BRDF^{\vec{i}_0,\vec{r}}$	Bidirectional reflectivity Distribution function	sr^{-1}	T	True temperature	K
C_1	First Planck constant $= 1.19 \times 10^8$	$\mathrm{W}\,\mu\mathrm{m}^4\,\mathrm{m}^{-2}$	$T_L^{\vec{i}_0}$	Radiance temperature	K
C_2	Second Planck constant $= 1.44 \times 10^4$	$K\ \mu$m	u, v	Pixels coordinates	

[1] R. Reichle, P. Andrew, C. Balorin, B. Brichard, S. Carpentier, Y. Corre, M. Davi, R. Daviot, C. Desgranges, J. Gardarein, E. Gauthier, D. Guilhem, S. Gicquel, A. Herrmann, D. Hernandez, M. Jouve, C. L. Niliot, T. Loarer, A. Martin, J. Martins, J.-B. Migozzi, J. Patterlini, C. Pocheau, F. Rigollet, H. Roche, and J. Travere, J. Nucl. Mater. **390–391**, 1081 (2009).
[2] B. Rousseau, J. Brun, D. Meneses, and P. Echegut, Int. J. Thermophys. **26**, 1277 (2005).
[3] F. Meriaudeau, Image Vis. Comput. **25**, 1124 (2007).
[4] T. Pierre, B. Remy, and A. Degiovanni, J. Appl. Phys. **103**, 034904 (2008).
[5] C.-D. Wen and I. Mudawar, Int. Commun. Heat Mass Transfer **33**, 1063 (2006).
[6] T. Duvaut, Infrared Phys. Technol. **51**, 292 (2008).
[7] V. S. Dozhdikov and A. V. Petrov, High Temp. -High Press. **27/28**, 403 (1995).
[8] M. Broussely, A. Levick, and G. Edwards, J. Phys. IV (France) **125**, 627 (2005).
[9] I. Alxneit, Sol. Energy **85**, 516 (2011).
[10] T. P. Salikhov and V. Kan, Appl. Sol. Energy **39**, 66 (2003).
[11] D. Y. Svet, AIP Conf. Proc. **684**, 681–686 (2003).
[12] D. Hernandez, J. Badie, F. Escourbiac, and R. Reichle, Fusion Eng. Des. **83**, 672 (2008).
[13] D. Hernandez, J. Sanz, A. Netchaieff, P. Ridoux, and V. Le Sant, Measurement **42**, 836 (2009).
[14] B. T. Phong, Commun. ACM **18**, 311 (1975).
[15] D. Hernandez, Rev. Sci. Instrum. **76**, 024904 (2005).
[16] Y. Rotrou, T. Sentenac, Y. Le Maoult, P. Magnan, and J. Farré, QIRT J. **3**, 93 (2006).
[17] J.-J. Orteu, Y. Rotrou, T. Sentenac, and L. Robert, Exp. Mech. **48**(2), 163 (2008).
[18] P. Saunders, Metrologia **34**, 201 (1997).
[19] P. Saunders and D. R. White, Metrologia **40**, 195 (2003).
[20] D. A. Haner, B. T. McGuckin, R. T. Menzies, C. J. Bruegge, and V. Duval, Appl. Opt. **37**, 3996 (1998).